

Three-Dimensional Invisibility to Superscattering Induced by Zeeman-Split Modes

Grigorios P. Zouros

*Section of Condensed Matter Physics, National and Kapodistrian University of Athens,
Panepistimioupolis, GR-157 84 Athens, Greece and*

School of Electrical and Computer Engineering, National Technical University of Athens, GR-157 73 Athens, Greece

Georgios D. Kolezas

School of Electrical and Computer Engineering, National Technical University of Athens, GR-157 73 Athens, Greece

Evangelos Almpanis

*Section of Condensed Matter Physics, National and Kapodistrian University of Athens,
Panepistimioupolis, GR-157 84 Athens, Greece and*

*Institute of Nanoscience and Nanotechnology, NCSR “Demokritos”,
Patriarchou Gregoriou and Neapoleos Street, Ag. Paraskevi, GR-153 10 Athens, Greece*

Kosmas L. Tsakmakidis

*Section of Condensed Matter Physics, National and Kapodistrian
University of Athens, Panepistimioupolis, GR-157 84 Athens, Greece*

(Dated: August 4, 2020)

We report that the fundamental three-dimensional (3-D) scattering single-channel limit can be overcome in magneto-optical assisted systems by inducing nondegenerate magnetoplasmonic modes. In addition, we propose a 3-D active (magnetically assisted) forward-superscattering to invisibility switch, functioning at the same operational wavelength. Our structure is composed of a high-index dielectric core coated by indium antimonide (InSb), a semiconductor whose permittivity tensorial elements may be actively manipulated by an external magnetic bias \mathbf{B}_0 . In the absence of \mathbf{B}_0 , InSb exhibits isotropic epsilon-near-zero (ENZ) and plasmonic behavior above and below its plasma frequency, respectively, a frequency band which can be utilized for attaining invisibility using cloaks with permittivity less than that of free space. With realistic B_0 magnitudes as high as 0.17 T, the gyroelectric properties of InSb enable the lift of mode degeneracy, and the induction of a Zeeman-split type dipolar magnetoplasmonic mode that beats the fundamental single-channel limit. This all-in-one design allows for the implementation of functional and highly tunable optical devices.

Dynamically manipulating the scattering characteristics of resonant structures comprises a valuable platform for the development of functional, tunable optical devices enabling a variety of applications [1, 2], including optical sorting [3], visible-to-invisible switching [4], cloaking-to-superscattering switching [5], directionality inversion [6–8], all-optical switching [9], multipolar interference [10], quantum emitters [11], or light-matter interaction enhancement at the subwavelength regime via superscattering operation [12]. A pathway to actively manipulating the scattering response is through external-agent based alteration of the material properties of the structure, which retains the geometry and operational wavelength fixed. Techniques to achieve this dynamic switching between different states include the electrically configurable liquid crystal based meta-optic devices which change the phase or the orientation of the surrounding liquid crystal [13], the use of phase-change materials that allow for a permittivity change by transiting between amorphous and crystalline states using external laser beams [14], magneto-optical media whose permittivity can be modified by an external magnetic bias [15], ferromagnetic materials whose permeability can be manipulated via temperature variations [16], or ultrafast nonlinear op-

tical switching based on light-induced change of a material’s dielectric permittivity (normally, to low values) [17].

In this work, we demonstrate that in optimized 3-D core-shell spherical particles consisting of a high-index dielectric core and an InSb semiconductor coating, we can overcome the fundamental single-channel limit of the scattering efficiency [18], by appropriately inducing a magnetoplasmonic resonance. In addition, while keeping the geometry and operational wavelength fixed, we can transform the configuration to an invisible state simply by switching off the external magnetic field \mathbf{B}_0 , utilizing the dynamic properties of the structure’s active semiconductor coating, InSb, whose permittivity can be manipulated by relatively small or modest values of \mathbf{B}_0 . In the presence of low B_0 magnitudes, the coating exhibits gyroelectric along with plasmonic activity, resulting in the induction of magnetoplasmonic modes [19, 20] which—different from recent two-dimensional (2-D) superscattering schemes [12]—are here nondegenerate, i.e., of Zeeman-split type [8, 21, 22]. We show that these nondegenerate magnetoplasmonic resonances exhibit strong directional scattering. In the absence of \mathbf{B}_0 , and for the same operational wavelength, InSb exhibits isotropic

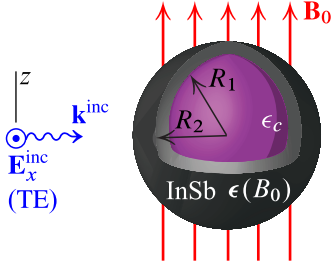


FIG. 1. Schematic representation of the proposed set-up. Linear TE polarized light impinges at an angle of 90° with respect to the external magnetic field \mathbf{B}_0 .

ENZ and plasmonic behavior above and below its plasma frequency, respectively, a frequency band that can be utilized for attaining invisibility [23, 24]. This *off-to-on* transition from invisibility to superscattering operation is robust under material losses and gives rise to a huge enhancement in the scattering efficiency. The findings obtained from our formal analytical solution are in excellent agreement with full-wave simulations (COMSOL), thereby establishing the validity of the proposed set-up.

In Fig. 1 we show the configuration of the forward-superscattering to invisibility magnetic switch. The main structure consists of a R_1 -radius high permittivity $\epsilon_c = 20\epsilon_0$ dielectric core—with ϵ_0 being the free space permittivity—coated by a R_2 -radius shell consisting of semiconductor InSb. The whole configuration is exposed in external magnetic field $\mathbf{B}_0 = B_0\mathbf{e}_z$. Since \mathbf{B}_0 is z -oriented, InSb's permittivity tensor is expressed in cartesian coordinates by $\epsilon(B_0) = \epsilon_1(B_0)(\mathbf{e}_x\mathbf{e}_x^T + \mathbf{e}_y\mathbf{e}_y^T) + i\epsilon_2(B_0)(\mathbf{e}_x\mathbf{e}_y^T - \mathbf{e}_y\mathbf{e}_x^T) + \epsilon_3(B_0)\mathbf{e}_z\mathbf{e}_z^T$ —where T denotes transposition—with $\epsilon_1(B_0) = \epsilon_0\epsilon_\infty\{1 - (\omega + iv)\omega_p^2/\omega/[(\omega + iv)^2 - \omega_c^2]\}$, $\epsilon_2(B_0) = \epsilon_0\epsilon_\infty\{\omega_c\omega_p^2/\omega/[(\omega + iv)^2 - \omega_c^2]\}$ and $\epsilon_3(B_0) = \epsilon_0\epsilon_\infty[1 - \omega_p^2/\omega/(\omega + iv)]$ [25]. In the aforementioned relations we have used realistic material parameters where $\epsilon_\infty = 15.6$ accounts for interband transitions, $\omega_p = (N_e e^2/\epsilon_0/\epsilon_\infty/m^*)^{1/2} = 4\pi \times 10^{12}$ rad/s is the plasma angular frequency (with N_e the electron density, e the elementary charge and $m^* = 0.0142m_e$ electron's effective mass, where m_e is electron's rest mass), $\omega_c = eB_0/m^*$ is cyclotron angular frequency, and $v = 0.001\omega_p$ the damping angular frequency which accounts for losses. In case of null \mathbf{B}_0 , InSb turns isotropic with $\epsilon_1(0) \equiv \epsilon_3(0)$ and $\epsilon_2(0) = 0$. In addition, the core-shell structure is nonmagnetic and it is located in free space. The set-up is illuminated by a normal to \mathbf{B}_0 impinging transverse electric (TE) plane wave—i.e., the incident electric field \mathbf{E}^{inc} is normal to the plane of incidence, therefore, if the plane of incidence is the yz -plane as shown in Fig. 1, then \mathbf{E}^{inc} is x -polarized. To examine the electromagnetic (EM) response of the magnetic switch proposed in this work, the solution of EM plane wave scattering by dielectric-gyroelectric core-shell spheres is necessary. This is feasible by the discrete eigenfunction method employed in [26, 27] for homogeneous

spheres and spheroids. In the Supplemental Material [28] we extend that method and we rigorously develop a full-wave analytical solution of EM scattering by dielectric-gyroelectric spheres. The scattering efficiency is given by

$$Q_{sc} = \frac{\lambda_0^2}{\pi} \sum_{m=-n}^n \sum_{n=1}^{\infty} (|a_{mn}|^2 + |b_{mn}|^2), \quad (1)$$

where λ_0 is the free space wavelength, a_{mn} , b_{mn} the expansion coefficients of the scattered electric field [28, Eq. (S2)], and m , n the spherical harmonics and angular momentum indices, respectively. In the long wavelength limit, the spectrum is dominated by the electric dipolar (ED) and magnetic dipolar (MD) responses for which $n = 1$. In particular, for purely isotropic scatterers, the ED response to the scattering efficiency is obtained when only the b_{11} expansion coefficient contributes in Eq. (1), while the MD response stems exclusively from a_{11} .

When the MD response is negligible and the ED response dominates the spectrum, transparency can be achieved by utilizing an isotropic lossless ENZ coating with permittivity $\epsilon_1 < \epsilon_0$ and a radii ratio determined by [23]

$$\frac{R_1}{R_2} = \left[\frac{(\epsilon_1 - \epsilon_0)(2\epsilon_1 + \epsilon_c)}{(\epsilon_1 - \epsilon_c)(2\epsilon_1 + \epsilon_0)} \right]^{1/3}. \quad (2)$$

By appropriately selecting ϵ_1 , ϵ_c , Eq. (2) yields the radii ratio for which cancellation of the ED term to the spectrum is achieved. Eq. (2) is ideally suited for lossless and non-dispersive materials. To make a rough estimation of a possible transparency window, using Eq. (2), we neglect losses by setting zero damping term v in Drude-Lorentz model of InSb, we set $\epsilon_1 = 0.4929\epsilon_0$ as an average value of ϵ_1 in the range from 2 THz to 2.065 THz, and along with $\epsilon_c = 20\epsilon_0$, Eq. (2) yields $R_1/R_2 = 0.650$. This radii ratio can serve as a tentative basis also in our case, where the InSb coating is lossy and dispersive.

At first, we examine the optical response of the lossy and dispersive core-shell particle in the absence of \mathbf{B}_0 , where InSb is isotropic. By employing the radii ratio $R_1/R_2 = 0.650$, we obtain the spectrum shown in Fig. 2(a). In blue line we show the total normalized Q_{sc} which involves all terms of Eq. (1), up to an index n_{max} for which convergence is ensured. In addition, we also depict the separate MD/ED and electric quadrupolar (EQ) terms. The latter one contributes to Eq. (1) by employing only the a_{12} expansion coefficient. The ED/MD resonances appearing in the range from $\lambda_0/R_2 = 5$ up to $\lambda_0/R_2 = 7$ in Fig. 2(a), are typical subwavelength resonances due to the high-index dielectric core. On the contrary, the EQ/ED peaks above $\lambda_0/R_2 = 7.5$ are plasmonic resonances of the coating. This is because at frequencies below the plasma frequency $f_p = \omega_p/(2\pi)$, InSb changes its properties from ENZ to plasmonic. This is

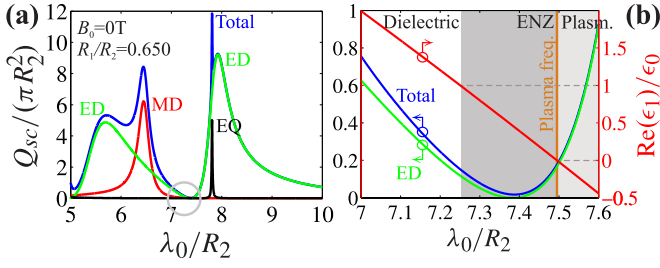


FIG. 2. Achieving ENZ- and plasmonic-based transparency under null \mathbf{B}_0 in the set-up of Fig. 1 with $\epsilon_c = 20\epsilon_0$, $R_2 = 20 \mu\text{m}$ and $R_1/R_2 = 0.650$. (a) Spectrum in the sub-wavelength regime. Blue: total normalized Q_{sc} ; red: MD term; green: ED term; black: EQ term. The gray circle indicates the region where transparency is achieved. (b) Zoom in the λ_0/R_2 window indicated by the gray circle in (a). Blue/left axis: total normalized Q_{sc} ; green/left axis: ED term; red/right axis: $\text{Re}(\epsilon_1)/\epsilon_0$ of the InSb coating above and below plasma frequency $f_p = 2$ THz (shown by the vertical orange line at $\lambda_0/R_2 = 7.495$). White region (dielectric): $\text{Re}(\epsilon_1)/\epsilon_0 > 1$; dark-gray region (ENZ): $0 < \text{Re}(\epsilon_1)/\epsilon_0 < 1$; bright-gray region (plasmonic): $\text{Re}(\epsilon_1)/\epsilon_0 < 0$.

illustrated in Fig. 2(b) which focuses in the transition region indicated by the gray circle in Fig. 2(a). There, the two domains (ENZ/plasmonic) are marked by dark-gray and bright-gray colors, the boundary of which is determined by the plasma frequency at $\lambda_0/R_2 = 7.495$ (or $f_p = 2$ THz). The real part of the coating permittivity $\text{Re}(\epsilon_1)$ depends almost linearly on the wavelength, as shown in Fig. 2(b). In particular, $\text{Re}(\epsilon_1)/\epsilon_0 = 0$ at $\lambda_0/R_2 = 7.495$ (which corresponds to frequency f_0 equal to f_p), while $\text{Re}(\epsilon_1)/\epsilon_0 \approx 1$ at $\lambda_0/R_2 = 7.25$ ($f_0 = 2.068$ THz). In brief, Fig. 2(b) indicates that inside the ENZ region of the coating, the normalized Q_{sc} from solely the ED contribution (which is similar to the total normalized Q_{sc}) is suppressed, resulting in a respective transparency window. However, as we shall see below, this is not the case when $\mathbf{B}_0 \neq 0$.

In Fig. 3(a) we show the map of the normalized Q_{sc} , versus the external B_0 magnitude, in the same wavelength window as the one in Fig. 2(b). All the other parameters of the configuration are the same with the ones used in Fig. 2. The deep blue region at $B_0 = 0$ T in Fig. 3(a) corresponds to the transparency window discussed in Fig. 2(b), where normalized Q_{sc} is almost zero. By *switching on* the external magnetic field, and varying its magnitude, we can monitor the impact that it has on this transparency window. In particular, for $B_0 \neq 0$ T, sharp peaks in intense red color appear, which correspond to high Q_{sc} values. In Fig. 3(b) we plot the normalized Q_{sc} for two particular choices of B_0 , i.e., $B_0 = 0$ and $B_0 = 0.17$ T. The first case ($B_0 = 0$) is already discussed but shown for comparison. At $B_0 = 0.17$ T, two dominant scattering modes appear, where the longer-wavelength one has greater normalized Q_{sc} than the

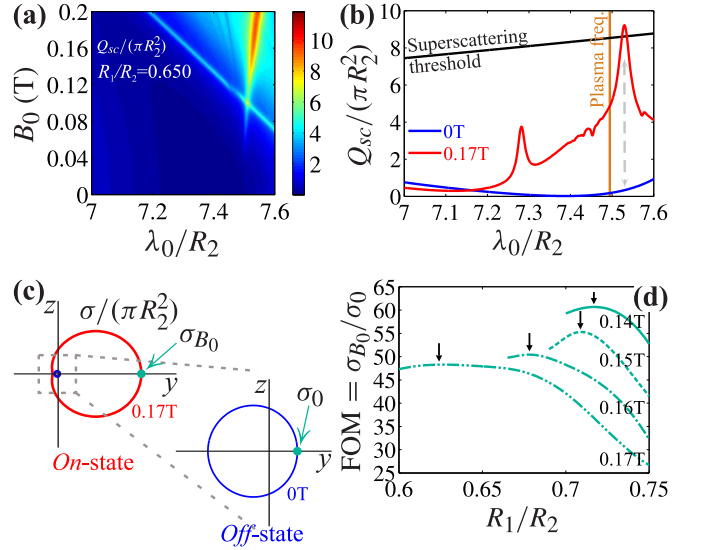


FIG. 3. Application of external \mathbf{B}_0 and 2-D optimization. The set-up is the same as in Fig. 2. (a) Total normalized Q_{sc} vs B_0 and λ_0/R_2 in the transparency-enabled λ_0/R_2 window as indicated by Fig. 2(b). (b) Comparison of total normalized Q_{sc} between null and non-null external \mathbf{B}_0 states. Blue: $B_0 = 0$ T; red: $B_0 = 0.17$ T; black: superscattering threshold. The gray dashed arrowhead line depicts the precise $\lambda_0/R_2 = 7.530$ of the *off-on* transition. (c) Normalized σ on yz -plane when the structure operates at $\lambda_0/R_2 = 7.530$. Red: *on-state*/forward-superscattering for $B_0 = 0.17$ T; blue: *off-state*/transparency for $B_0 = 0$ T. (d) 2-D optimization of FOM vs B_0 and R_1/R_2 . The small arrows indicate the optimal states at which FOM is maximized.

dipole-superscattering single-channel threshold given by [18]

$$\frac{Q_{sc}}{\pi R_2^2} = \frac{3}{2\pi^2} \left(\frac{\lambda_0}{R_2}\right)^2. \quad (3)$$

The corresponding dipole-superscattering threshold is shown in Fig. 3(b) in black. As shown, the superscattering resonance at $\lambda_0/R_2 = 7.530$ can be dramatically suppressed by *switching off* the external magnetic field, where the particle becomes almost transparent. This transition from superscattering operation— $Q_{sc}/(\pi R_2^2) = 9.223$ ($B_0 = 0.17$ T) to almost transparency— $Q_{sc}/(\pi R_2^2) = 0.3339$ ($B_0 = 0$ T), controlled entirely by the external magnetic bias, is pointed out with a dashed arrow in Fig. 3(b). In Fig. 3(c) we depict the radiation pattern of the structure when the latter operates exactly at $\lambda_0/R_2 = 7.530$, by plotting the normalized bistatic scattering cross section $\sigma(\theta, \varphi)/(\pi R_2^2)$ on yz -plane by varying $\theta \in [0, \pi]$, for the two different B_0 values that allow for the *on-off* switching. When $B_0 = 0.17$ T, the coated particle operates at a forward-superscattering state with $\sigma_{B_0}/(\pi R_2^2) \equiv \sigma(\theta = \pi/2, \varphi = \pi/2)/(\pi R_2^2) = 20.45$, i.e., the value of $\sigma/(\pi R_2^2)$ in the forward direction. Contrariwise, when $B_0 = 0$ T, the particle is at *off-state*/transparency with the respective point

in the suppressed radiation pattern being $\sigma_0/(\pi R_2^2) \equiv \sigma(\theta = \pi/2, \varphi = \pi/2)/(\pi R_2^2) = 0.4269$. We point out here that the lower-wavelength and smaller in amplitude resonance in Fig. 3(b) at $\lambda_0/R_2 = 7.282$, when $B_0 = 0.17$ T, is much below the single-channel limit. Additionally, this mode does not exhibit unidirectional scattering. In particular, this resonance shows a poor $\sigma_{B_0}/(\pi R_2^2) = 5.48$ while, at the same instance, it has non negligible backscattering response $\sigma(\theta = \pi/2, \varphi = 3\pi/2)/(\pi R_2^2) = 2.08$ rendering it improper for the application studied here.

Next, we define a figure of merit (FOM) as the ratio

$$\text{FOM} = \frac{\sigma_{B_0}}{\sigma_0}. \quad (4)$$

For the specific example of Fig. 3(c), FOM is not optimized, and yields $\text{FOM} = 47.90$. In Fig. 3(d) we show that for a given B_0 there exists an optimal R_1/R_2 ratio for which FOM is maximized, yet the superscattering state is maintained. This is regarded as a 2-D optimization of FOM vs B_0 and R_1/R_2 . Fig. 3(d) shows four constant- B_0 curves of FOM vs R_1/R_2 for 0.14 T, 0.15 T, 0.16 T and 0.17 T. All values in Fig. 3(d) correspond to greater normalized Q_{sc} than the fundamental single-channel limit. For the preceding example of $B_0 = 0.17$ T, optimal FOM is achieved at $R_1/R_2 = 0.625$. The other maximum values shown by the arrows in Fig. 3(d) correspond to $R_1/R_2 = 0.675$ ($B_0 = 0.16$ T), $R_1/R_2 = 0.705$ ($B_0 = 0.15$ T) and to $R_1/R_2 = 0.715$ ($B_0 = 0.14$ T).

In Fig. 4 we demonstrate the realization of the invisibility to superscattering magnetic switch for the optimized structure ($R_1/R_2 = 0.675$) at $B_0 = 0.16$ T. Fig. 4(a) depicts the total normalized Q_{sc} for the *on*-state operation, along with its dipolar components. Higher-order terms—such as quadrupolar—are negligible in this regime. We note in passing that, for an isotropic spherical particle, the m -mode index in Eq. (1) is degenerate, which means that a multipolar mode of electric or magnetic type is only characterized by the angular momentum index n . However, this is not the case for gyroelectric spherical particles, as in the present case, where the lifting of the m -degeneracy leads to $2n + 1$ separate Zeeman-split modes [21, 22]. Since in the λ_0/R_2 regime of Fig. 4(a) only the dipolar ($n = 1$) modes exist, we expect three ($2n + 1 = 3$) nondegenerate modes for each dipolar (parent) mode, with indices $m = 0, \pm 1$. However, the coupling of each one of such modes with the external radiation strongly depends on the angle of incidence and polarization [21, 29]. Our full-wave analytical calculations reveal that, in the specific spectral window of Fig. 4(a), for light impinging as shown in Fig. 1, we have $a_{\pm 1,1} = b_{0,1} = b_{1,1} = 0$ while the nonzero expansion coefficients are only $a_{0,1}$ and $b_{-1,1}$ and yield nondegenerate MD and ED modes, respectively. The contribution of $a_{0,1}$ and $b_{-1,1}$ to the normalized Q_{sc} is depicted in Fig. 4(a) by the red and green curves, respectively. As evident,

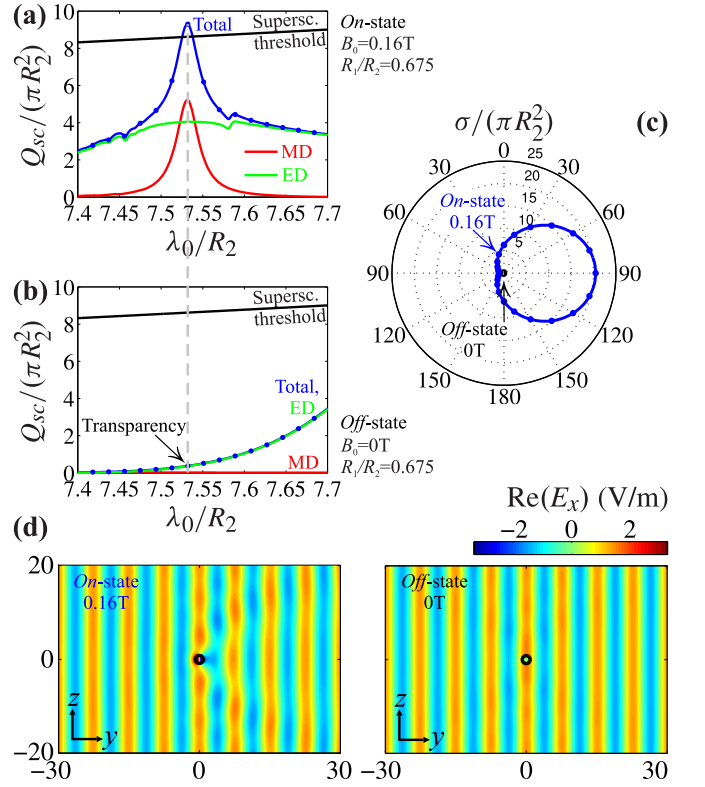


FIG. 4. Engineering the magnetic switch for optimal operation at $R_1/R_2 = 0.675$ and $B_0 = 0.16$ T. The other values of parameters are the same as in Fig. 2. (a) Spectrum in *on*-state/superscattering operation with $B_0 = 0.16$ T. Blue: total normalized Q_{sc} /curve: our method/dots: COMSOL; red: MD term due to $a_{0,1}$; green: ED term due to $b_{-1,1}$; black: superscattering threshold. (b) Spectrum in *off*-state/transparency operation with $B_0 = 0$ T. Blue: total normalized Q_{sc} /curve: our method/dots: COMSOL; red: MD term; green: ED term; black: superscattering threshold.. The gray dashed vertical line depicts the value $\lambda_0/R_2 = 7.532$ where the optimal *off-on* transition takes place. (c) Radiation pattern of normalized σ on yz -plane under $\lambda_0/R_2 = 7.532$ excitation. Blue: *on*-state/forward superscattering when $B_0 = 0.16$ T/curve: our method/dots: COMSOL; black: *off*-state/transparency when $B_0 = 0$ T. (d) Near-field of $\text{Re}(E_x)$ on yz -plane under *on*-state (left) and *off*-state (right) activity.

the high peak at $\lambda_0/R_2 = 7.532$ beats the superscattering limit. The physical mechanism behind this scattering maximization is attributed to the overlapping—as shown by the dashed gray line—of the nondegenerate $m = 0$ MD and $m = -1$ ED contributions, and is understood as a magnetoplasmon polariton excited in the magnetized InSb coating [30, 31]. Obviously, this is not the case when InSb is not magnetized, as in the case of Fig. 2(a) where the coating exhibits purely plasmonic properties and the spectrum is dominated by degenerate ED/EQ resonances only. We note in passing that, the plasmonic Fano feature [32] at $\lambda_0/R_2 = 7.587$ —as shown in Fig. 4(a)—is attributed to the nondegenerate $m = -1$ ED contribution, where a similar asymmetric feature has been also

observed in ring-type cavities [33]. The respective spectrum at *off*-state is shown in Fig. 4(b), using the same scale as the one in Fig. 4(a). At $\lambda_0/R_2 = 7.532$, the system is almost transparent with normalized Q_{sc} being significantly suppressed at $Q_{sc}/(\pi R_2^2) = 0.3746$. With a $Q_{sc}/(\pi R_2^2) = 9.302$ when $B_0 = 0.16$ T, this *off*-to-*on* transition results to a 2383% enhancement in Q_{sc} . Fig. 4(c) depicts the radiation pattern when the system operates at $\lambda_0/R_2 = 7.532$. The forward-superscattering operation is achieved with a FOM = 50.38 and an almost null radiation pattern when $B_0 = 0$ T. To validate our findings, we fully compare our analytical solution with COMSOL's finite-element solver. The total normalized Q_{sc} , as obtained by our method, is in full agreement with COMSOL, with the latter being depicted by the blue dots in Figs 4(a)–(c). To have a degree of comparison, our method yields $Q_{sc}/(\pi R_2^2) = 9.302$ and 0.3746 at the magnetoplasmonic resonance and at the transparency state, respectively, when $\lambda_0/R_2 = 7.532$. COMSOL's respective values are $Q_{sc}/(\pi R_2^2) = 8.892$ and 0.3746 while the superscattering threshold is $Q_{sc}/(\pi R_2^2) = 8.622$. In addition, the radiation pattern depicted in Fig. 4(c) is in full agreement with COMSOL. Fig. 4(d) depicts the $\text{Re}(E_x)$ on yz -plane for *on*- and *off*-state activity. Fig. 4(d)/right confirms the invisibility state since the incoming wave passes through the scatterer almost unperturbed, while the snapshot in Fig. 4(d)/left clearly illustrates the forward-scattering propagation along the positive y -axis.

In conclusion, based on a rigorous analytical solution of the 3-D EM scattering problem by dielectric-gyroelectric spheres, corroborated by full-wave simulations, we introduced a high-permittivity/semiconductor structure for breaking the fundamental single-channel limit of the scattering efficiency. This operation is established by inducing nondegenerate dipolar magnetoplasmonic modes, in the subwavelength regime, by operating the structure below the semiconductor's plasma frequency, and by applying a low external magnetic bias in the range 0.14 T–0.17 T. Likewise, for the same operational wavelength and core-shell radii, for which superscattering operation occurs, we have also shown how 3-D invisibility can be attained, simply by turning off the external magnetic field. The latter effect stems from the dynamic properties of the coating, which change to a plasmonic behaviour in the absence of magnetic field, enabling a plasmonic based cloak. By a 2-D optimization relative to the external magnetic field and the radii ratio, we identified optimal states for which the *on-off* ratio of the forward scattering cross sections is maximized, with a concurrent enormous enhancement in the total scattering efficiency. Our findings could pave the way towards the design of highly functional and tunable optical devices, including state-of-the-art optical metasurfaces [34].

G.P.Z., E.A., and K.L.T. were supported by the General Secretariat for Research and Technology (GSRT)

and the Hellenic Foundation for Research and Innovation (HFRI) under Grant No. 1819.

-
- [1] A. I. Kuznetsov, A. E. Miroshnichenko, M. L. Brongersma, Y. S. Kivshar, and B. Luk'yanchuk, *Science* **354**, aag2472 (2016).
 - [2] K. L. Tsakmakidis, O. Hess, R. W. Boyd, and X. Zhang, *Science* **358**, eaan5196 (2017).
 - [3] D. A. Shilkin, E. V. Lyubin, M. R. Shcherbakov, M. Lapine, and A. A. Fedyanin, *ACS Photonics* **4**, 2312 (2017).
 - [4] M. V. Rybin, K. B. Samusev, P. V. Kapitanova, D. S. Filonov, P. A. Belov, Y. S. Kivshar, and M. F. Limonov, *Phys. Rev. B* **95**, 165119 (2017).
 - [5] Y. Huang, Y. Shen, C. Min, and G. Veronis, *Opt. Mat. Expr.* **8**, 1672 (2018).
 - [6] T. J. Arruda, A. S. Martinez, and F. A. Pinheiro, *Phys. Rev. A* **94**, 033825 (2016).
 - [7] M. Q. Liu, C. Y. Zhao, and B. X. Wang, *Nanoscale* **10**, 18282 (2018).
 - [8] G. P. Zouros, G. D. Kolezas, E. Almpanis, K. Baskourellos, T. Stefański, and K. L. Tsakmakidis, *Nanophotonics* (2020), accepted for publication. DOI: 10.1515/nanoph-2020-0223.
 - [9] M. R. Shcherbakov, P. P. Vabishchevich, A. S. Shorokhov, K. E. Chong, D.-Y. Choi, I. Staude, A. E. Miroshnichenko, D. N. Neshev, A. A. Fedyanin, and Y. S. Kivshar, *Nano Lett.* **15**, 6985 (2015).
 - [10] M. F. Limonov, M. V. Rybin, A. N. Poddubny, and Y. S. Kivshar, *Nature Photon.* **11**, 543 (2017).
 - [11] A. F. Cihan, A. G. Curto, S. Raza, P. G. Kik, and M. L. Brongersma, *Nature Photon.* **12**, 284 (2018).
 - [12] C. Qian, X. Lin, Y. Yang, X. Xiong, H. Wang, E. Li, I. Kaminer, B. Zhang, and H. Chen, *Phys. Rev. Lett.* **122**, 063901 (2019).
 - [13] A. Komar, Z. Fang, J. Bohn, J. Sautter, M. Decker, A. Miroshnichenko, T. Pertsch, I. Brener, Y. S. Kivshar, I. Staude, and D. N. Neshev, *Appl. Phys. Lett.* **110**, 071109 (2017).
 - [14] S. Lepeshov, A. Krasnok, and A. Alù, *ACS Photonics* **6**, 2126 (2019).
 - [15] W. J. M. Kort-Kamp, F. S. S. Rosa, F. A. Pinheiro, and C. Farina, *Phys. Rev. Lett.* **111**, 215504 (2013).
 - [16] T. J. Arruda, A. S. Martinez, and F. A. Pinheiro, *Phys. Rev. A* **92**, 023835 (2015).
 - [17] L. Caspani, R. P. M. Kaipurath, M. Clerici, M. Ferrera, T. Roger, J. Kim, N. Kinsey, M. Pietrzyk, A. D. Falco, V. M. Shalaev, A. Boltasseva, and D. Faccio, *Phys. Rev. Lett.* **116**, 233901 (2016).
 - [18] M. I. Tribelsky and B. S. Luk'yanchuk, *Phys. Rev. Lett.* **97**, 263902 (2006).
 - [19] S. Chen, F. Fan, X. He, M. Chen, and S. Chang, *Applied optics* **54**, 9177 (2015).
 - [20] J. Chochol, K. Postava, M. Čada, and J. Pištora, *Scientific Reports* **7**, 1 (2017).
 - [21] E. Almpanis, *Phys. Rev. B* **97**, 184406 (2018).
 - [22] E. Almpanis, G. P. Zouros, P. A. Pantazopoulos, K. L. Tsakmakidis, N. Papanikolaou, and N. Stefanou, *Phys. Rev. B* **101**, 054412 (2020).
 - [23] A. Alù and N. Engheta, *Phys. Rev. E* **72**, 016623 (2005).
 - [24] K. L. Tsakmakidis, O. Reshef, E. Almpanis, G. P. Zouros,

- E. Mohammadi, D. Saadat, F. Sohrabi, N. Fahimi-Kashani, D. Etezzad, R. W. Boyd, and H. Altug, *Nat. Commun.* **10**, 4859 (2019).
- [25] K. L. Tsakmakidis, L. Shen, S. A. Schulz, X. Zheng, J. Upham, X. Deng, H. Altug, A. F. Vakakis, and R. W. Boyd, *Science* **356**, 1260 (2017).
- [26] J. L.-W. Li and W.-L. Ong, *IEEE Trans. Antennas Propag.* **59**, 3370 (2011).
- [27] G. D. Kolezas, G. P. Zouros, and K. L. Tsakmakidis, *IEEE J. Sel. Top. Quantum Electron.* **25**, 4700912 (May/June 2019).
- [28] See Supplemental Material for details on the development of the rigorous analytical solution.
- [29] P. Varytis and N. Stefanou, *J. Opt. Soc. Am. B* **33**, 1286 (2016).
- [30] J. J. Brionand, R. F. Wallis, A. Hartstein, and E. Burstein, *Phys. Rev. Lett.* **28**, 1455 (1972).
- [31] L. Xia, X. Zhang, D. Wang, W. Zhang, and J. Han, *Opt. Commun.* **446**, 84 (2019).
- [32] B. Luk'yanchuk, N. I. Zheludev, S. A. Maier, N. J. Halas, P. Nordlander, H. Giessen, and C. T. Chong, *Nature Mat.* **9**, 707 (2010).
- [33] F. Hao, Y. Sonnefraud, P. V. Dorpe, S. A. Maier, N. J. Halas, and P. Nordlander, *Nano Lett.* **8**, 3983 (2008).
- [34] D. Neshev and I. Aharonovich, *Light Sci. Appl.* **7**, 1 (2018).